

X Persei: A study on the origin of its high-energy emission

J. Rodi¹, L. Natalucci¹, and M. Fiocchi¹

INAF - Istituto di Astrofisica e Planetologia Spaziali, via Fosso del Cavaliere 100; 00133 Roma, Italy

e-mail: james.rod@inaf.it

Received XXX; accepted XXX

ABSTRACT

Aims. The origin of the hard X-ray emission in the Be/X-ray binary system X Persei has long been debated as its atypical ‘two-hump’ spectrum can be modelled in multiple ways. The main debate focuses on the the high-energy hump, which is fit as either a cyclotron resonance scatter frequency (CRSF) or inverse Comptonization due to bulk Comptonization.

Methods. Using INTEGRAL/JEM-X and ISGRI data, we studied the temporal and spectral variability in the 3 – 250 keV energy range during observations over ~ 15 years. A NuSTAR observation was also included in a joint spectral fit with the INTEGRAL spectrum.

Results. We find that the joint spectrum can be described well by a low-energy component due to thermal Comptonization and a high-energy component due to bulk Comptonization, a CRSF, or a cyclotron emission line. The three models begin to diverge above ~ 120 keV, where statistics are low.

Conclusions. We compare our results with observations of other Be/X-ray binaries that show similar ‘two-hump’ spectra while in a low-luminosity state. As the sources are in a low accretion state, the bulk Comptonization process is likely inefficient, and thus not an explanation for the high-energy component. The broad CRSF (27 ± 2 keV) in X Persei suggests that the high-energy emission is not due to a CRSF. Thus, the high-energy component is potentially due to cyclotron emission, though other scenarios are not definitively excluded.

Key words. individual: X Persei – X-rays: Binaries – stars: Neutron

1. Introduction

The X-ray source 4U 0352+309 was first detected by the *Uhuru* satellite (Giacconi et al. 1972) and was later found to be the companion of the Be star X Persei (X Per) (Braes & Miley 1972; van den

Bergh 1972). The X-ray source has a pulse period of ~ 837 s (White et al. 1976; Haberl et al. 1998), indicating that the compact object is a neutron star (Delgado-Martí et al. 2001). The system has an orbital period of approximately 250 days and has an inclination of $\sim 26^\circ - 33^\circ$ (Delgado-Martí et al. 2001). Distances to the system range from 0.7 – 0.95 kpc (Lyubimkov et al. 1997; Roche et al. 1997; Telting et al. 1998). *Gaia* Data Release 3 reports a distance of 0.69 kpc.

Broadband observations at X-rays have predominately focused on understanding the emission process(es) responsible for the ‘two-hump’ spectrum. Using *BeppoSAX*, Di Salvo et al. (1998) described the spectrum as a thermal radiation component and a non-thermal partially Comptonization cyclotron line or high-temperature thermal bremsstrahlung. Coburn et al. (2001) analyses with *RXTE* fit the spectrum as a blackbody spectrum with a power law modified by a cyclotron resonance scattering frequency (CRSF). INTERNATIONAL Gamma-Ray Astrophysics Laboratory (INTEGRAL) results from Lutovinov et al. (2012) described the spectrum with a high-energy cut-off power law with a CRSF. The thermal component is below the energy threshold, and thus was not included in the analysis.

In contrast, a different INTEGRAL analysis reported that the spectrum can be fit as a thermal and bulk Comptonization model (Doroshenko et al. 2012). *Suzaku* results provided intensity-dependent differences when fitting the spectra to the physically motivated compag model (Farinelli et al. 2012). Using *Suzaku* data, Maitra et al. (2017) found that the average and lower intensity spectra can be described well by just the compag model, but higher-flux spectra require a CRSF component.

Though the origin of the spectral shape remains debated, similar two-hump spectra have been reported in other sources (1A 0535+262 Tsygankov et al. (2019b), GRO J1008–57 Lutovinov et al. (2021), and GX 304–1 Tsygankov et al. (2019a)) while in a low-luminosity state ($\sim 10^{34-35}$ erg/s). Sokolova-Lapa et al. (2021) presented an alternative model to explain the GX 304–1 spectrum as a low-energy hump due to a thermal component and a high-energy component due to resonant Comptonization. Thus, the process(es) at work in those sources is/are likely the same as in X Per, which has been observed at the same luminosity level (White et al. 1976; Lyubimkov et al. 1997; Di Salvo et al. 1998; Coburn et al. 2001; La Palombara & Mereghetti 2007; Lutovinov et al. 2012; Maitra et al. 2017).

In this work, we investigate INTEGRAL observations over the course of the mission (~ 15 years) to search for spectral variability and differentiate between previously proposed physical models for Be/X-ray binaries in a low-luminosity state.

2. Observations and data reduction

INTEGRAL was launched into an elliptical orbit in October 2002 from Baikonur, Kazakhstan (Jensen et al. 2003). The instruments on board INTEGRAL have observed X Per numerous times during the course of the mission, providing a long baseline of observations. In this work, we analyzed INTEGRAL observations using data from the Joint European Monitor for X-rays (JEM-X)

(Lund et al. 2003) and the INTEGRAL on-board Imager (IBIS) (Ubertini et al. 2003). The data span INTEGRAL revolutions 170 – 2122 (MJD 53069 – 58702). There are 1327 IBIS observations (science windows) during this period for a total exposure time of 2250 ks and 364 science windows (scw) with JEM-X for a total exposure time of 830 ks. JEM-X has fewer observations due to its smaller field of view (FoV) compared to IBIS and the fact that many observations including X Per do not have the source as the main target.

The JEM-X and IBIS/ISGRI (INTEGRAL Soft Gamma-Ray Imager) analyses were performed using the standard Offline Science Analysis (OSA) tools developed for INTEGRAL data.¹ Following the JEM-X Analysis User Manual, JEM-X spectral analysis was performed using *jemx_science_analysis* (v11.1) with 49 channels in the 3 – 20 keV energy range. For ISGRI, spectral analysis was performed using the routine *ibis_science_analysis* (v11.2), as is documented in the IBIS Analysis User Manual. The spectra were extracted in 28 channels in the 30 – 250 keV energy range. Average spectra for each instrument were generated using the OSA tool *spe_pick*. A 1% systematic error was added, as is suggested for standard analyses.

For NuSTAR, the data are from observation 30401033002, corresponding to 2019-01-01 10:26:09 to 2019-01-02 20:11:09 UTC. As is outlined in the NuSTAR Data Analysis Software Guide,² data reduction for FPMA and FPMB was performed with the *nuproducts* routine using *nustards_01Apr_v1.9.2* and CALDB version 2022-01-29. The total exposure time is 38.4 ks. For image analysis, the source extraction used a 116 arcsec circular region and a 142 arcsec background circular region. Spectra were generated in the 3 – 70 keV energy range and rebinned to 800 bins (FPMA) and 782 bins (FPMB) to maximize the signal-to-noise ratio at high energies.

3. Results

3.1. Temporal results

The long-term light curves of JEM-X and ISGRI are shown in Figure 1. The points are on an INTEGRAL revolution timescale ($\sim 2 - 3$ days). This timescale maximizes the signal-to-noise ratio when searching for long-term spectral variability below in Sec 3.2.1. The JEM-X points are shown as blue stars. The ISGRI points are shown as black diamonds. The NuSTAR 3 – 79 keV count rates for FPMA and FPMB are 14.50 ± 0.02 and 13.96 ± 0.02 ct/s, respectively, and are plotted as red (FPMA) and green (FPMB) triangles. The errors are $\pm 1\sigma$, as are all subsequent errors. The NuSTAR count rates have been normalized by a factor of 0.5. The average JEM-X count rate is shown as a dotted blue line. The average ISGRI count rate is shown as a dash-dotted black line. The value of 0 ct/s is shown as a solid black line.

X Per shows temporal variability over the course of the mission and was significantly detected up to 100 keV by INTEGRAL. The average count rates (and significances) in JEM-X are 3.11 ± 0.02 ct/s (202.8σ) and 0.73 ± 0.01 ct/s (52.3σ) in the 3 – 10 keV and 10 – 20 keV energy bands,

¹ <https://www.isdc.unige.ch/integral/analysis#Software>

² https://heasarc.gsfc.nasa.gov/docs/nustar/analysis/nustar_swguide.pdf

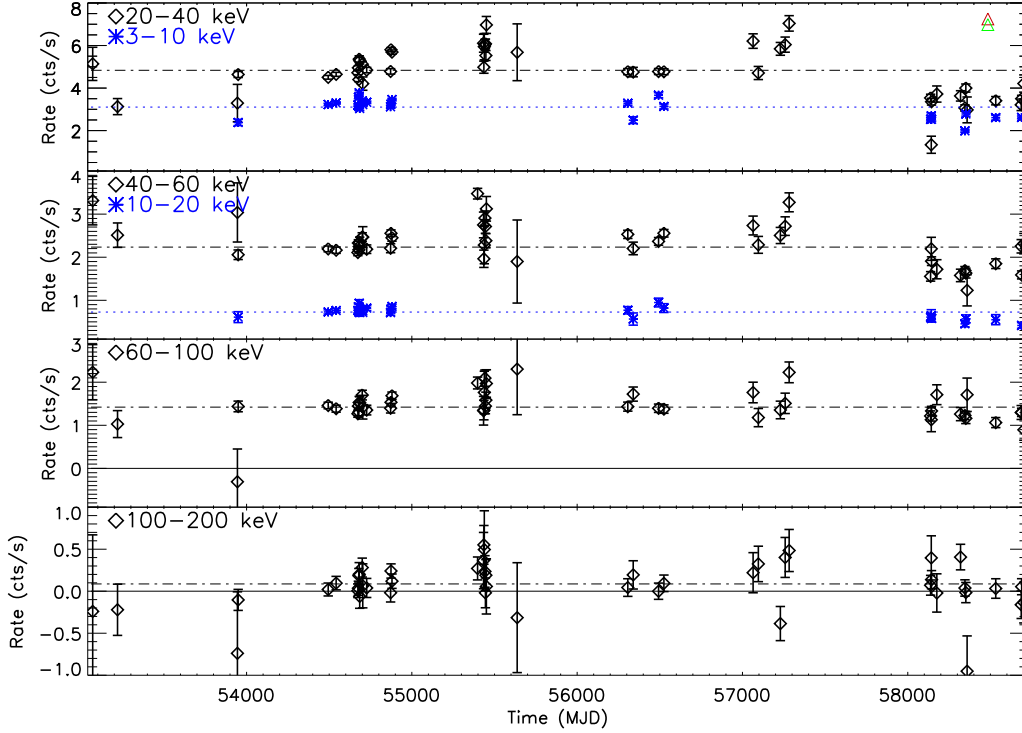


Fig. 1: X Per long-term light curve with JEM-X in the 3 – 10 keV and 10 – 20 keV energy bands as blue stars, and ISGRI in the 20 – 40 keV, 40 – 60 keV, 60 – 100 keV, and 100 – 200 keV energy bands. The average JEM-X count rate is shown as a dotted blue line. The average ISGRI count rate is shown as a dash-dotted black line. The value of 0 cts/s is shown as a solid black line. The *NuSTAR* 3 – 79 keV count rates are shown as a red and green triangles and have been normalized by a factor of 0.5.

respectively. The ISGRI count rates (and significances) are 4.84 ± 0.02 ct/s (200.0σ), 2.23 ± 0.02 ct/s (128.0σ), 1.42 ± 0.02 ct/s (74.4σ) in the 20 – 40 keV, 40 – 60 keV, and 60 – 100 keV energy bands, respectively. The source is marginally detected at 4.5σ in the 100 – 200 keV energy band with 0.09 ± 0.02 ct/s.

3.2. Spectral results

3.2.1. Spectra variability

To search for spectral variability on a revolution timescale ($\sim 2-3$ d), we fitted joint JEM-X/ISGRI spectra using XSPEC version 12.9.0. Previous works on X Per modelled the spectrum as a power law with a high-energy cut-off (powerlaw*highcut) modified by a CRSF (gabs) (Coburn et al. 2001; Lutovinov et al. 2012). Thus, we fitted the spectra with an nthcomp*gabs model as it

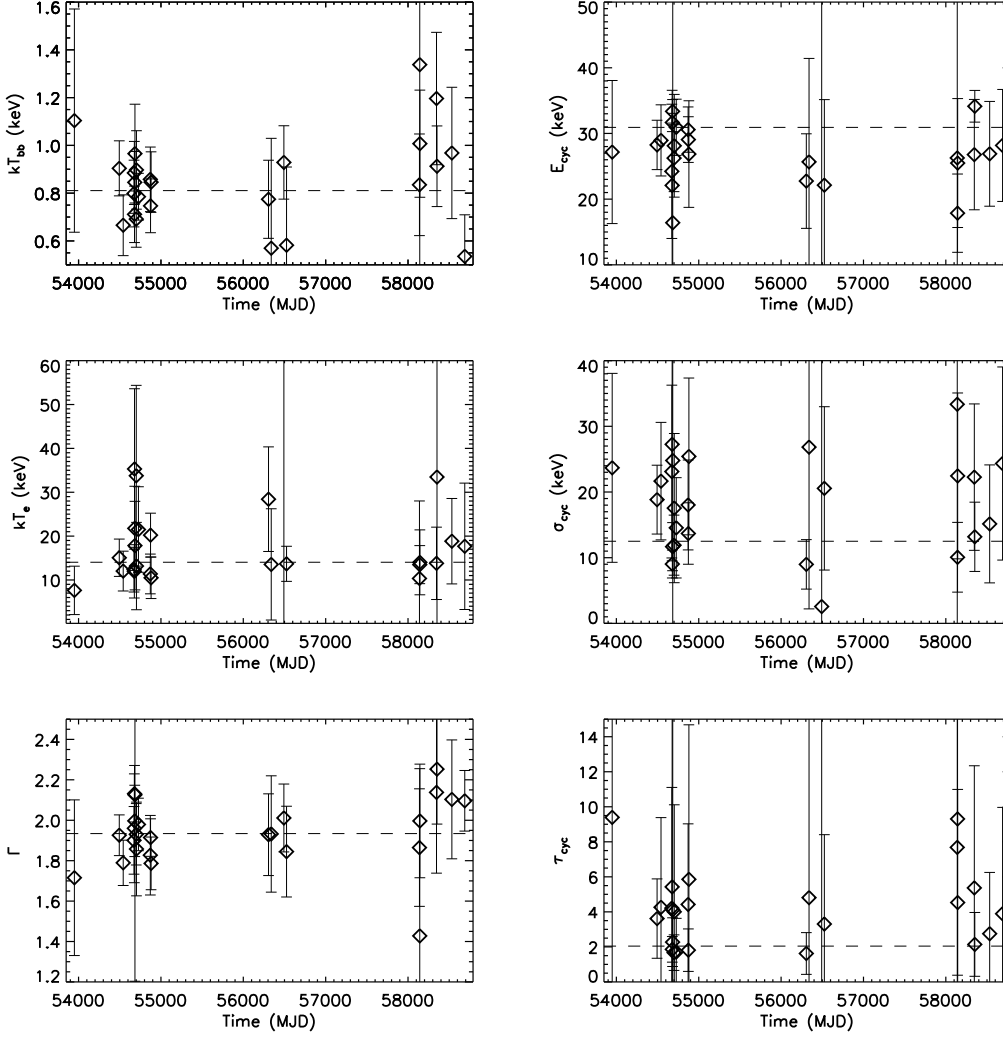


Fig. 2: Evolution of X Per best-fit parameters to a `nthcomp*gabs` model on a revolution timescale. The weighted average value is overplotted as a dashed line in each panel.

provides a more physically motivated continuum spectrum with the same number of free parameters. In Sec 3.2.2 below, we evaluate the merits of different spectral models. Figure 2 shows the revolution timescale parameters with the continuum parameters in the first column and the `gabs` parameters in the second column. The average values for each parameter are plotted as a dashed line in each panel. The disk blackbody (kT_{bb}), electron temperature (kT_e), and the power law index (Γ) appear constant with average values of 0.81 ± 0.03 keV, 14 ± 1 keV, and 1.93 ± 0.03 , respectively. The `gabs` parameters show a similar behavior with no clear long-term variability in the cyclotron energy, line width, or optical depth, respectively. The average values are $E_{cyc} = 30.9 \pm 0.8$ keV, $\sigma_{cyc} = 12 \pm 1$ keV, and $\tau_{cyc} = 2.0 \pm 0.4$. However, the errors on the parameters of an individual revolution timescale are often large due to relatively short exposure times.

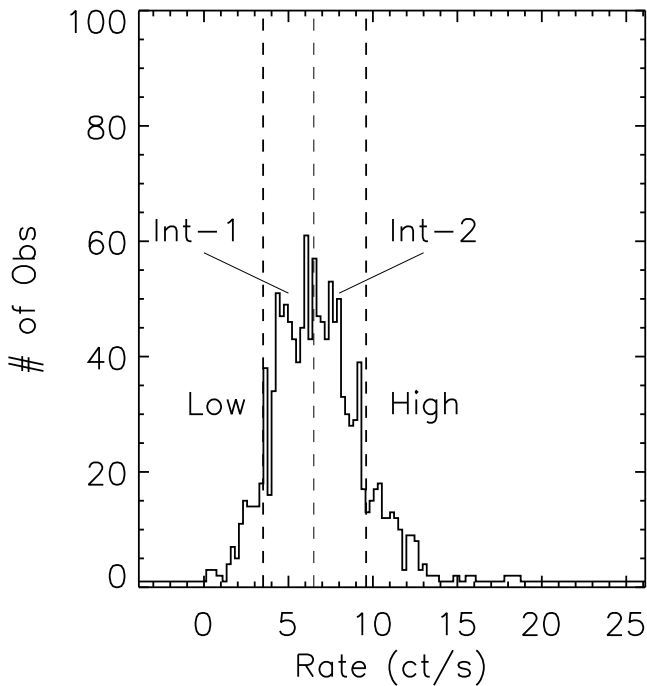


Fig. 3: Histogram of the 20 – 80 keV count rate with dashed lines denoting low, intermediate-1, intermediate-2, and high count-rate levels.

For the JEM-X spectra, the exposure time varies from $\sim 7.7 - 66$ ks. For the ISGRI spectra, the exposure time varies from $\sim 10 - 125$ ks.

To reduce the fit parameter errors, we built a count-rate histogram using the 20 – 80 keV count rate (Figure 3), as Maitra et al. (2017) and grouped the data into four count-rate levels: low, intermediate-1, intermediate-2, and high. As an initial test, we fitted the spectra to the *nthcomp* model. In each case, the spectrum was poorly described by the model with χ^2/ν values of $137.90/67 = 2.06$, $390.13/67 = 5.82$, $460.21/67 = 6.87$, and $242.67/67 = 3.62$ for the low, intermediate-1, intermediate-2, and high count-rate levels, respectively. Subsequently, we fitted the spectra using the *nthcomp***gabs* model and found that each spectrum is described well by the data (See Table 1). We also tested the need for an additional component (that is modelled with *gabs*) using *simftest* in Xspec for each count-rate level. Using 1,000 iterations, the fit did not improve in any of the realizations. Thus, an additional component is required at a level of $\gtrsim 3.3\sigma$ (1/1000). The best-fit parameters for the *nthcomp***gabs* model are listed in Table 1. The best-fit parameters versus the mean count rate within a bin are plotted in Figure 4. The average fit parameters are plotted as a dashed line in each panel.

The continuum parameters (kT_{bb} , kT_e , Γ) do not show any significant dependence on flux, though the errors during the low flux period are large. A positive correlation between flux and cyclotron absorption energy has been reported in a number of sources (e.g. Staubert et al. (2007); Klochkov et al. (2012); DeCesar et al. (2013); Fürst et al. (2014); Sartore et al. (2015)); thus, the presence of such a correlation would support an interpretation of a CRSF in X Per. However, the cyclotron absorption parameters (E_{cyc} , σ_{cyc} , and τ_{cyc}) also do not exhibit significant flux evolution.

Table 1: Count-rate level fit parameters with Tbags*(nthcomp*gabs)

	Low	Intermediate-1	Intermediate-2	High
kT_{bb}	1.1 ± 0.2 keV	0.87 ± 0.05 keV	0.85 ± 0.05 keV	0.9 ± 0.7 keV
kT_e	16 ± 8 keV	12 ± 3 keV	12 ± 2 keV	14 ± 2 keV
Γ	2.1 ± 0.6	2.1 ± 0.1	1.9 ± 0.7	1.88 ± 0.06
E_{cyc}	20 ± 17 keV	20 ± 7 keV	24 ± 4 keV	27 ± 3 keV
σ_{cyc}	25 ± 15 keV	31 ± 9 keV	27 ± 6 keV	21 ± 5 keV
τ_{cyc}	3 ± 4	3 ± 3	2 ± 1	1.3 ± 0.9
red. χ^2/ν	0.90/64	0.83/64	0.59/64	0.77/64

-nthcomp mode: kT_{bb} is the seed photon temperature, kT_e is the electron temperature, and Γ is the power law index.

-gabs model: E_{cyc} , σ_{cyc} , and τ_{cyc} are the energy, width, and optical depth of the CRSF line, respectively.

The E_{cyc} values are consistent with the average value. We fitted the data to a linear model. The best-fit slope was 0.9 ± 1.0 (shown as a red line in the top panel of the second column of Figure 4), consistent with a slope of 0. Therefore, we consider the X Per spectrum to be constant during *INTEGRAL* observations in this work.

There is a 10 keV gap between JEM-X and ISGRI (20 – 30 keV). To bridge this energy range, spectra from a *NuSTAR* observation were included. As a test of agreement between the instruments, we fitted the average *INTEGRAL* spectra with the *NuSTAR* spectra and found a red. $\chi^2/d.o.f.$ = 0.99/1647. Thus, the four spectra are in good agreement. The instrument cross-normalizations were $C_{JEM-X} = 1.05 \pm 0.01$, $C_{FPM A} = 0.965 \pm 0.008$, and $C_{FPM B} = 0.944 \pm 0.008$. The ISGRI cross-normalization was fixed to 1. The fit results are discussed in the subsequent section.

3.2.2. Average spectrum

Due to the uncertain nature of the hard X-ray emission, the source has been studied by multiple missions over the past decades. Results can generally be grouped into models using two additive components (Di Salvo et al. 1998; Doroshenko et al. 2012) and models with a CRSF (Coburn et al. 2001; Lutovinov et al. 2012; Maitra et al. 2017). We began with spectral fits to the JEM-X/ISGRI/*NuSTAR* data using phenomenological models. A fit to an absorbed power law model with a cross-instrument normalization constant*Tbags*powerlaw found $\Gamma = 2.095 \pm 0.001$ (red. $\chi^2/d.o.f.$ = 14.11/1650). nH was fixed to 0.15×10^{22} cm⁻² based on Coburn et al. (2001). The residuals are complex, with the model over-predicting the observed flux < 5 keV, between 10 – 40 keV, and > 90 keV, suggesting the presence of a cut-off power law continuum spectrum or possibly a more complex continuum. An absorbed cut-off power law model finds best-fit parameters of $\Gamma = 1.879 \pm 0.002$, a cut-off energy with $E_C = 6.6 \pm 0.1$ keV, and a fold energy of $E_{fold} = 36.8 \pm 0.5$ keV (red. $\chi^2/d.o.f.$ = 8.99/1648). The residuals show that the model again over-predicts the observed flux at energies similar to the power law model.

Table 2: Phenomenological continuum spectrum parameters

Tbabs*(powerlaw*highcut+powerlaw*highcut)		Tbabs*(powerlaw*highcut*gabs)	
Γ_1	0.80 ± 0.02	Γ	2.5 ± 0.6
E_{cut_1}	3.30 ± 0.05 keV	E_{cut}	5.7 ± 0.5 keV
E_{fold_1}	5.0 ± 0.1 keV	E_{fold}	17.8 ± 0.6 keV
Γ_2	1.40 ± 0.02	E_{cyc}	17.8 ± 0.6 keV
E_{cut_2}	70 ± 1 keV	σ_{cyc}	29.2 ± 0.8 keV
E_{fold_2}	23 ± 2 keV	τ_{cyc}	3.6 ± 0.3
red. χ^2/ν	1.11/1644		1.02/1645

-powerlaw mode: Γ is the power law index

-highcut model: E_{cut} is the cut-off energy, E_{fold} is the e-fold energy

-gabs model: E_{cyc} , σ_{cyc} , and τ_{cyc} are the energy, width, and optical depth of the CRSF line, respectively.

Following Di Salvo et al. (1998), we fitted the spectrum using a phenomenological two-component model with two power laws with high-energy cut-off components with low-energy and high-energy cut-offs. The `constant*Tbabs*(powerlaw*highcut+powerlaw*highcut)` fit finds similar parameters, which are listed in Table 2, and acceptably fit the data (red. $\chi^2/d.o.f = 1.11/1644$). The cross-normalization parameters relative to the ISGRI flux are $C_{JEM-X} = 1.05 \pm 0.01$, $C_{FPMA} = 0.967 \pm 0.008$, and $C_{FPMB} = 0.946 \pm 0.008$. Fits with subsequent models resulted in similar cross-normalization values. The JEM-X and ISGRI cross-normalizations are in good agreement. The *NuSTAR* cross-normalization values are close to 1. However, the spectra come from a single observation compared to the long-term average for ISGRI; thus, values different from 1 are unsurprising.

A model with two continuum components is able to adequately explain the spectrum. However, other authors (Coburn et al. 2001; Lutovinov et al. 2012; Maitra et al. 2017) have proposed that the dip feature is due to a CRSF instead of two different hard X-ray emission components. Thus, we fitted the spectrum to a `constant*Tbabs(powerlaw*highcut*gabs)` model. The best-fit parameters are similar to previous results and are given in Table 2; again, they describe the data well (red. $\chi^2/d.o.f = 1.02/1645$).

Next, we tried physically motivated models to explain the origin of the two ‘humps.’ Following the analysis of Doroshenko et al. (2012), we also fitted the data to a `CompTT+CompTT` model, which attributes the ‘humps’ to thermal Comptonization processes. In this model, the free parameters are the photon seed temperature (kT_0), the electron temperature (kT_e), and the optical depth (τ). A two `CompTT` model provides a statistically acceptable fit to the model (red. $\chi^2/d.o.f = 1.06/1646$) but is qualitatively worse, especially at high energies (see Figure 5 and discussion below.) The best-fit parameters are given in Table 3, as are the parameters for subsequent fits.

Becker & Wolff (2005a,b) proposed that accreting X-ray pulsar spectra are due to a combination of thermal and bulk Comptonization. Thus, we fitted the data with a `comptb+comptb` model Farinelli et al. (2008). In the `comptb` model, the free parameters are the seed temperature (kT_s), the seed photon spectral index (Γ), the Comptonization spectrum energy index (α), the efficiency

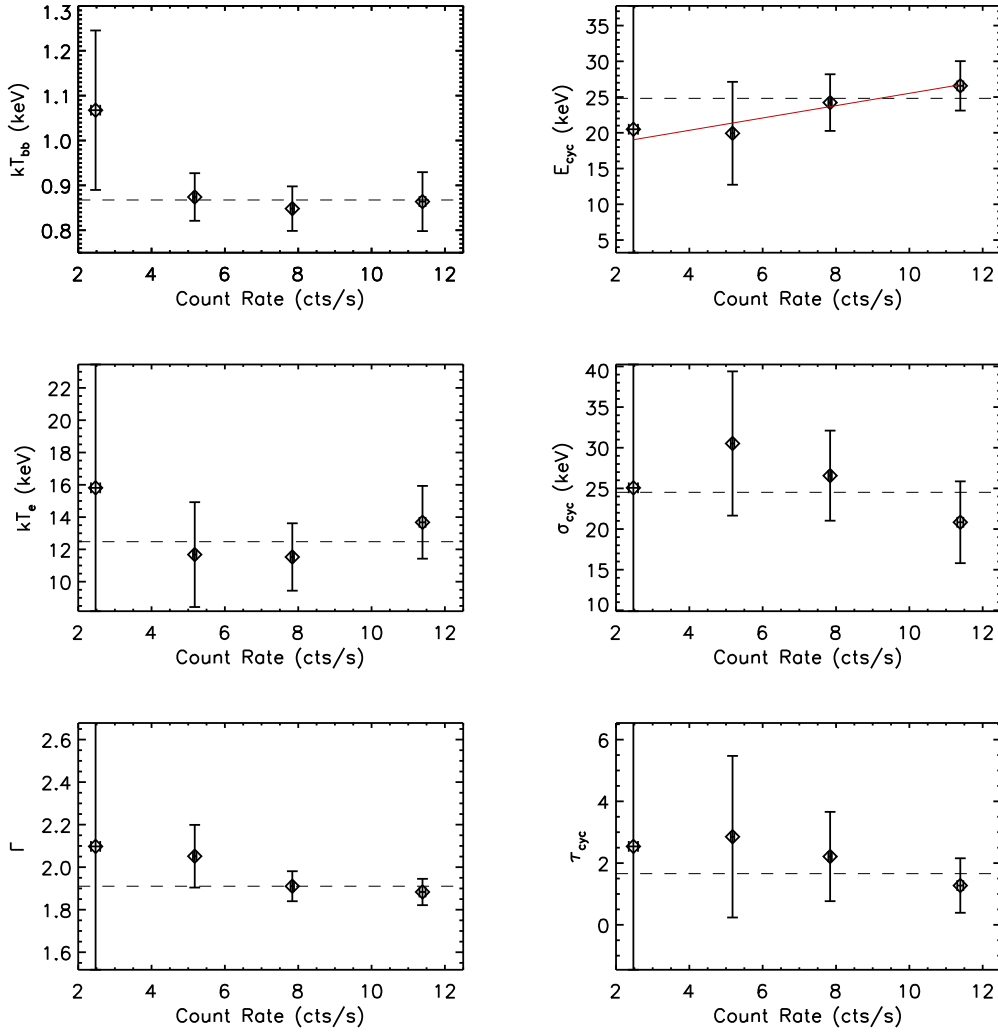


Fig. 4: Evolution of X Per best-fit parameters to a `nthcomp*gabs` model for different flux levels. The average values are overplotted as a dashed line in each panel. The red line in the E_{cyc} panel is a fit to the cyclotron energy vs count rate.

of the bulk Comptonization to the thermal Comptonization (δ), the electron temperature (kT_e), and the illumination factor (A), which is related to the fractional amount of seed photon radiation directly observed. An initial fit with all the parameters free is able to describe the data well (red. $\chi^2/d.o.f = 1.04/1638$), but none of the parameters are constrained. Following the analysis of accreting neutron stars in Farinelli et al. (2008), we fixed δ to 0 and A to 8 for a low-energy component due to thermal emission. In this scenario, the low-energy `comptb` model simplifies to the `ComptTT` model Farinelli et al. (2008). The model describes the data well (red. $\chi^2/d.o.f = 0.98/1644$) with significant bulk Comptonization found ($\delta = 13 \pm 2$), though the several of the parameters are unconstrained or poorly constrained. This model provides a better description of the data compared to the `ComptTT+ComptTT` model with $\Delta\chi^2 = 126.51$ with two fewer degrees of freedom.

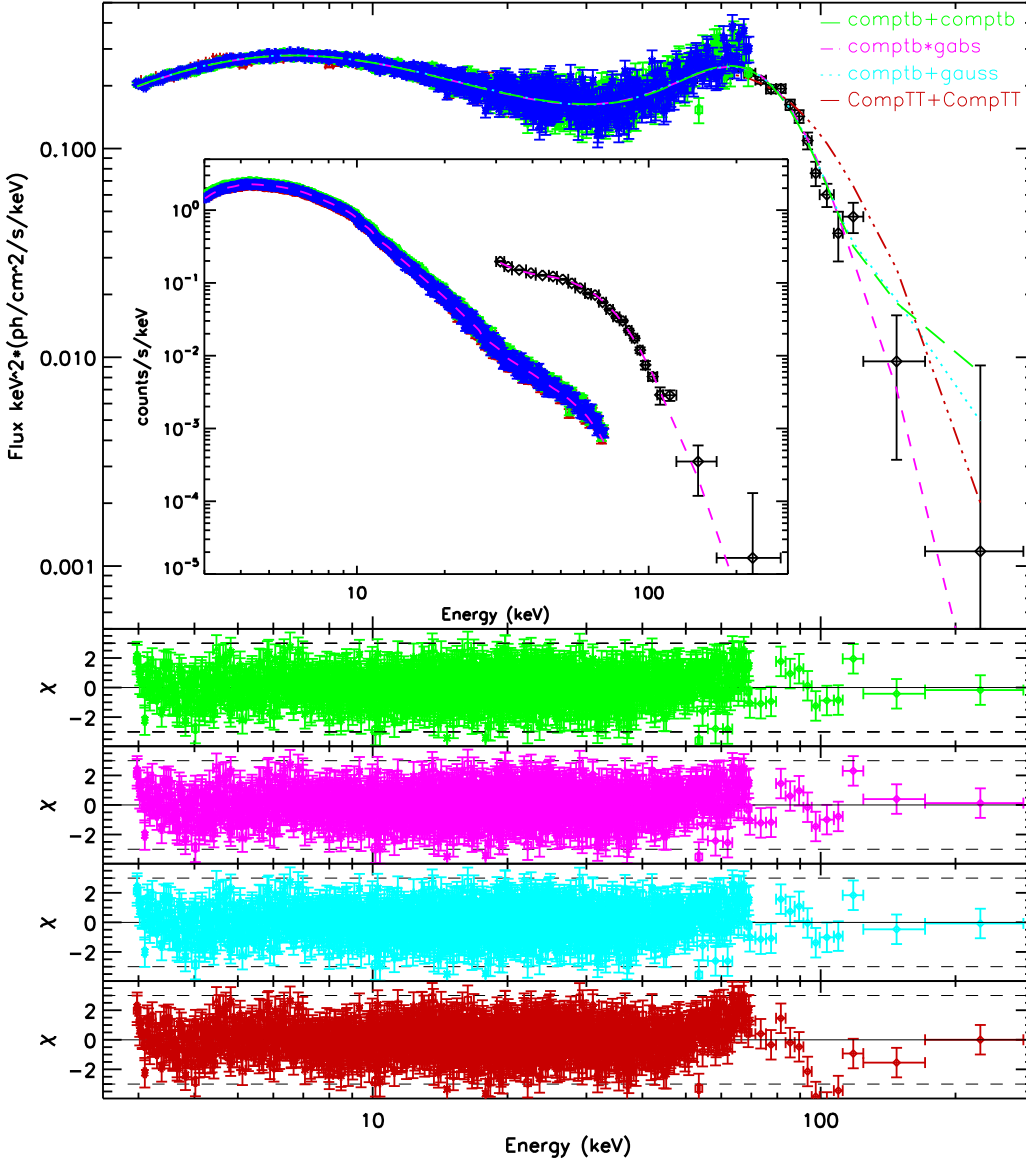


Fig. 5: X Per average spectrum with ISGRI (black diamonds), JEM-X (red triangles), *NuSTAR*/FPMA (blue stars), and FMPB (green squares). The best-fit models are overplotted with `comptb+comptb` (long green dashes), `comptb*gabs` (short magenta dashes), `comptb+gauss` (cyan dots), and `CompTT+CompTT` (red dots and dashes). The folded spectrum with the `comptb*gabs` model is shown as an inset. Plots of the residuals for the `comptb+comptb`, `comptb*gabs`, `comptb+gauss`, and `CompTT+CompTT` fits, respectively, are plotted in panels below the spectrum. Dashed lines are plotted at $\pm 3\sigma$.

Subsequently, we tested a `comptb*gabs` model to possibly explain the spectrum with CRSF. As before, δ was fixed to 0, and the log of the illumination was fixed to 8. The model also fits the data well (red. $\chi^2/d.o.f = 0.99/1646$). The CRSF model ($\chi^2/\nu = 1631.66/1646$) provides a better fit than the two `CompTT` model with $\Delta\chi^2 = 112.65$ with the same number of free parameters and a comparable χ^2 to `comptb+comptb` ($\Delta\chi^2 = -13.86$), though with two more free parameters.

Nelson et al. (1993) report that for low-luminosity accreting X-ray pulsars such as X Per, a broad cyclotron emission line may be present below the cyclotron energy. Thus, we fitted the data

Table 3: Physically motivated spectrum parameters

Tbabs*(comptb+comptb)		Tbabs*(comptt+comptt)		Tbabs*(comptb*gabs)		Tbabs*(comptb+gauss)	
kT_s	2.0 ± 0.2 keV	kT_{01}	0.57 ± 0.02 keV	kT_s	1.86 ± 0.01	kT_s	1.77 ± 0.05 keV
Γ_1	1.4 ± 0.8	kT_{e1}	2.25 ± 0.03 keV	Γ	1.58 ± 0.06	Γ	1.54 ± 0.04
α_1	1.8 ± 0.1	τ_1	8.3 ± 0.1	α	1.10 ± 0.04	α	1.55 ± 0.02
kT_{e1}	57 ± 92 keV	kT_{02}	14.7 ± 0.1 keV	kT_e	10.8 ± 1.0 keV	kT_e	28 ± 6 keV
Γ_2	1.2 ± 24.4	kT_{e2}	3.06 ± 0.03 keV	E_{cyc}	23 ± 1 keV	E_{gauss}	51.4 ± 0.8 keV
α_2	0.39 ± 0.05	τ_2	20.0 ± 0.5	σ_{cyc}	27 ± 2 keV	σ_{gauss}	21.4 ± 0.9 keV
kT_{e2}	4.2 ± 0.5 keV			τ_{cyc}	2.4 ± 0.7		
δ	13 ± 2						
red. χ^2/ν	0.98/1644		1.06/1646		0.99/1646		0.99/1646

-comptb model: kT_s is the seed photon temperature, Γ is the seed photon spectral index, α is the Comptonization spectrum energy index, kT_e is the electron temperature, and δ is the efficiency of the bulk Comptonization to the thermal Comptonization.

-comptt model: kT_0 is the seed photon temperature, kT_e is the electron temperature, and τ is the optical depth. E_{gauss} and σ_{gauss} are the energy and width of the cyclotron emission line, respectively.

-gabs model: E_{cyc} , σ_{cyc} , and τ_{cyc} are the energy, width, and optical depth of the CRSF line, respectively.

-gauss model: E_{gauss} and σ_{gauss} are the energy and width of the cyclotron emission line, respectively.

to a comptb+gauss model assuming that the second ‘hump’ is a cyclotron emission line instead of a cyclotron absorption line. As in the comptb*gabs model, delta was fixed to 0 and the log of the illumination was fixed to 8. Again, we find the data are described well by the model (red. $\chi^2/d.o.f = 0.98/1644$). The cyclotron emission line model ($\chi^2/\nu = 1625.63/1646$) provides a better fit than the two ComptTT model ($\Delta\chi^2 = 118.68$) for two more free parameters and a comparable χ^2 to the two comptb and comptb*gabs models with $\Delta\chi^2$ values of -7.83 and 6.03 , respectively, for the same number of free parameters.

The average spectrum and best-fit models are shown in Figure 5 with the ISGRI (black diamonds), JEM-X (red triangles), *NuSTAR*/FPMA (blue stars), and FMPB (green squares) data. The best-fit models are overplotted with comptb+comptb (long green dashes), comptb*gabs (short magenta dashes), comptb+gauss (cyan dots), and ComptTT+ComptTT (red dots and dashes). The folded spectrum with the comptb*gabs model is shown as an inset. The panels below the spectrum show the residuals to the comptb+comptb, comptb*gabs, comptb+gauss, and ComptTT+ComptTT fits, respectively. Dashed lines are plotted at $\pm 3\sigma$.

4. Discussion

4.1. Comparison of model results

In previous works, many of the analyses reporting a CRSF used only phenomenological models with a cut-off power law model. Because a cut-off power law model decreases differently from a Comptonization model (Petrucchi et al. 2001), we focused on physically motivated models to fit the average spectrum. Our fit to a two ComptTT model ($\chi^2/\nu = 1744.31/1646$) is able to describe the spectra well until ~ 95 keV. Above this energy, the model over-predicts the observed flux

(See Figure 5.), suggesting that the CompTT+CompTT model is unable to describe the high-energy spectrum.

The comptb+comptb model provides a better description of the data. This model found significant bulk Comptonization ($\delta = 13 \pm 2$), implying an optically thick environment and a high accretion rate (Tsygankov et al. 2019a), which is unlikely to be present in the low-luminosity state (Mushtukov et al. 2015). The model is above the observed data for the last two data points, but the errors on those points are large.

The CRSF model provides a better fit than the two CompTT model and comparable to the comptb+comptb. However, the broad cyclotron line ($\sigma = 27 \pm 2$ keV) is quite broad compared to typical cyclotron lines (Coburn et al. 2002; Staubert et al. 2019). This could be explained by an artificial broadening due to averaging over a variable E_{cyc} . As is shown in Figure 4, there is no long-term variability of the cyclotron line position. Additionally, phase analysis of the pulsar did not find significant variability in the line position (Coburn et al. 2001), which means short-term variability is not the cause of the broad cyclotron line.

Coburn et al. (2001) attribute the broadened line to viewing the source off-angle at $23 - 30^\circ$ (Delgado-Martí et al. 2001). They assume an electron temperature of ≥ 60 keV, using the best-fit parameter from a cut-off power law model, significantly lower than the $kT_e = 10.9$ keV found in this work. Using the equation from Meszaros & Nagel (1985), which accounts for broadening to thermalized electrons and Doppler broadening, with the values from our analysis, we find an expected width of roughly 3 keV, which is inconsistent with the 27 keV based on our spectral analysis. We note that the gabs parameters depend on the assumed continuum model.

Finally, the cyclotron emission line model provides a statistical fit comparable to the comptb+comptb and the CRSF models. However, the line energy (~ 51 keV) is significantly higher than predicted ($E_{gauss} \sim 5 - 20$ keV) (Nelson et al. 1995). In addition, Doroshenko et al. (2012) found that the high-energy component is more energetic than expected from Nelson et al. (1995).

The fundamental cyclotron energy can provide an estimate of the B-field using $E_B = 11.6B_{12}$ keV (ref). In the CRSF model, the fundamental cyclotron energy is 27 keV. In contrast, the fundamental cyclotron energy is roughly 51 keV. Thus, the B-field values are $\sim 2 \times 10^{12}$ G and $\sim 4 \times 10^{12}$ G for the CRSF and cyclotron emission line models, respectively. These values are similar to values reported for other accretion powered pulsars, which typically have a few $\times 10^{12}$ G (See Staubert et al. (2019); Kim et al. (2023)).

As is shown in Figure 5, the four models differ above ~ 90 keV. The CompTT+CompTT model is unable to describe the high-energy data, which disfavors that model. The three comptb models describe the data nearly equally well, with difficulties in each of their interpretations. Therefore, we are not able to differentiate between them based on our spectra, though higher significance results above ~ 120 keV could exclude some models.

4.2. Comparison with other sources

Recent results of Be/X-ray binaries during low-luminosity states have found spectra comparable X Per. These sources also exhibit significantly different luminosities to investigate how the spectra evolve. In the case of GX 304 – 1, using *Swift*/XRT and *NuSTAR* data, Tsygankov et al. (2019a) reported a comparable two-hump spectrum that they interpreted as likely due to either CRSF or cyclotron emission. Additionally, results of GRO J1008 – 57 with *SRGART-XC* and *NuSTAR* at different luminosities show an evolution of the spectrum, with the second hump becoming prominent at the lowest luminosity, which is consistent with a CRSF line at 80 – 90 keV (Lutovinov et al. 2021).

1A 0535 + 262 provides a different picture as its luminosity decreases. It shows a two-hump spectrum in its lowest luminosity like GRO J1008 – 57 and GX 304 – 1, but in *Swift*/XRT and *NuSTAR* the source also has an additional spectral feature modelled as a Gaussian at ~ 48 keV and a width of roughly 13 keV (Tsygankov et al. 2019b) that is not seen in the other sources. The presence of a cyclotron line suggests that the high-energy hump in 1A 0535+262 is not a CRSF and that the features seen in the other sources are also not CRSFs. As bulk Comptonization emission is unlikely to be efficient at the low accretion rates found in low-luminosity states since the required optical depths are not present (Mushtukov et al. 2015), Tsygankov et al. (2019a) excluded bulk Comptonization as an explanation for the high-energy hump in GX 304 – 1 during the source’s low-luminosity state. Thus, the authors interpreted the feature as a cyclotron emission line. They propose a scenario without the cold atmosphere assumption of Nelson et al. (1995).

5. Conclusions

In this work, we analyzed *INTEGRAL* observations from JEM-X and ISGRI spanning roughly 15.5 years. During this time, X Per displayed temporal variability in both instruments. A search for spectral variability using periods with both JEM-X and ISGRI did not find any significant variability in the 3–250 keV energy range on a revolution timescale. Also, an investigation of spectral variability at different count-rate levels (Figure 4) did not find any significant variability. Consequently, we created an average spectrum using all the *INTEGRAL* observations. This *INTEGRAL* spectrum was combined with a *NuSTAR* spectrum to study the different spectral models.

The origin of the hard X-ray emission in X Per has long been debated, with most of the discussion focused on the presence (or lack) of a CRSF line. In order to address this question, we focused on physical models, instead of phenomenological ones. The analysis found that the two-hump spectrum can be described well by `comptb+comptb`, `comptb*gabs`, and `comptb+gauss` models. A fit with `CompTT+CompTT` is statistically acceptable, but significantly over predicts the high-energy flux above ~ 90 keV.

The three `comptb` models result in comparably good fits; thus, we are not able to determine if the high-energy hump is due to Comptonization, cyclotron absorption, or cyclotron emission. However, the expected fluxes for the three models begin to diverge above approximately 120 keV

(See Figure 5). Thus, future observations to increase the high-energy statistics may be able to differentiate between the models.

Bulk Comptonization is unlikely to be efficient in such low-luminosity states as the accretion rate is low (Mushtukov et al. 2015). Thus, it is unlikely to be the origin of the high-energy emission in X Per. The observed width of the gabs feature is also significantly broader than expected for a CRSF interpretation, which disfavours a CRSF interpretation in the case of X Per. Therefore, we suggest that the high-energy hump seen in X Per is likely due to a cyclotron emission line.

Recent observations of other Be/X-ray binaries during low-luminosity states have found similar spectral shapes (GX 304–1, GRO J1008–57, and 1A 0535+262), indicating that the behavior seen in X Per is not unusual. Tsygankov et al. (2019b) results for 1A 0535+262 report a CRSF line on top of the high-energy hump, which suggests that the hump is not a cyclotron line, further supporting the interpretation of the high-energy feature in X Per and the other sources as being due to a cyclotron emission line.

Acknowledgements. The authors thank the referee for their comments and input. The authors thank the Italian Space Agency for the financial support under the “INTEGRAL ASI-INAF” agreement n° 2019-35-HH.0. The research leading to these results has received funding from the European Union’s Horizon 2020 Programme under the AHEAD2020 project (grant agreement n. 871158). This research has made use of data and/or software provided by the High Energy Astrophysics Science Archive Research Center (HEASARC), which is a service of the Astrophysics Science Division at NASA/GSFC. This work has made use of data from the European Space Agency (ESA) mission *Gaia* (<https://www.cosmos.esa.int/gaia>), processed by the *Gaia* Data Processing and Analysis Consortium (DPAC, <https://www.cosmos.esa.int/web/gaia/dpac/consortium>). Funding for the DPAC has been provided by national institutions, in particular the institutions participating in the *Gaia* Multilateral Agreement.

References

- Becker, P. A. & Wolff, M. T. 2005, *ApJ*, 621, L45.
- Becker, P. A. & Wolff, M. T. 2005, *ApJ*, 630, 465.
- Braes, L. L. E. & Miley, G. K. 1972, *Nature*, 235, 273.
- Coburn, W., Heindl, W. A., Gruber, D. E., et al. 2001, *ApJ*, 552, 738.
- Coburn, W., Heindl, W. A., Rothschild, R. E., et al. 2002, *ApJ*, 580, 394.
- DeCesar, M. E., Boyd, P. T., Pottschmidt, K., et al. 2013, *ApJ*, 762, 61.
- Delgado-Martí, H., Levine, A. M., Pfahl, E., et al. 2001, *ApJ*, 546, 455.
- Di Salvo, T., Burderi, L., Robba, N. R., et al. 1998, *ApJ*, 509, 897.
- Doroshenko, V., Santangelo, A., Kreykenbohm, I., et al. 2012, *A&A*, 540, L1.
- Farinelli, R., Titarchuk, L., Paizis, A., et al. 2008, *ApJ*, 680, 602.
- Farinelli, R., Romano, P., Mangano, V., et al. 2012, *MNRAS*, 424, 2854.
- Fürst, F., Pottschmidt, K., Wilms, J., et al. 2014, *ApJ*, 780, 133.
- Giacconi, R., Murray, S., Gursky, H., et al. 1972, *ApJ*, 178, 281.
- Haberl, F., Angelini, L., Motch, C., et al. 1998, *A&A*, 330, 189.
- Jensen, P. L., Clausen, K., Cassi, C. et al. 2003, *A&A*, 411, L7.
- Kim, V., Izmailova, I., & Aimuratov, Y. 2023, *ApJS*, 268, 21.
- Klochkov, D., Doroshenko, V., Santangelo, A., et al. 2012, *A&A*, 542, L28.
- La Palombara, N. & Mereghetti, S. 2007, *A&A*, 474, 137.
- Lund, N., Budtz-Jørgensen, C., Westergaard, N. J., et al. 2003, *A&A*, 411, L231.
- Lutovinov, A., Tsygankov, S., & Chernyakova, M. 2012, *MNRAS*, 423, 1978.
- Lutovinov, A., Tsygankov, S., Molokov, S., et al. 2021, *ApJ*, 912, 17.
- Lyubimkov, L. S., Rostopchin, S. I., Roche, P., et al. 1997, *MNRAS*, 286, 549.

- Maitra, C., Raichur, H., Pradhan, P., et al. 2017, MNRAS, 470, 713.
- Meszaros, P. & Nagel, W. 1985, ApJ, 298, 147.
- Mushtukov, A. A., Suleimanov, V. F., Tsygankov, S. S., et al. 2015, MNRAS, 447, 1847.
- Nelson, R. W., Salpeter, E. E., & Wasserman, I. 1993, ApJ, 418, 874.
- Nelson, R. W., Wang, J. C. L., Salpeter, E. E., et al. 1995, ApJ, 438, L99.
- Petrucchi, P. O., Haardt, F., Maraschi, L., et al. 2001, ApJ, 556, 716.
- Roche, P., Larionov, V., Tarasov, A. E., et al. 1997, A&A, 322, 139
- Sartore, N., Jourdain, E., & Roques, J. P. 2015, ApJ, 806, 193.
- Sokolova-Lapa, E., Gornostaev, M., Wilms, J., et al. 2021, A&A, 651, A12.
- Staubert, R., Shakura, N. I., Postnov, K., et al. 2007, A&A, 465, L25.
- Staubert, R., Trümper, J., Kendziorra, E., et al. 2019, A&A, 622, A61.
- Telting, J. H., Waters, L. B. F. M., Roche, P., et al. 1998, MNRAS, 296, 785.
- Tsygankov, S. S., Rouco Escorial, A., Suleimanov, V. F., et al. 2019, MNRAS, 483, L144.
- Tsygankov, S. S., Doroshenko, V., Mushtukov, A. A., et al. 2019, MNRAS, 487, L30.
- Ubertini, P., Lebrun, F., Cocco, G. D., et al. 2003, 139
- van den Bergh, S. 1972, Nature, 235, 273.
- White, N. E., Mason, K. O., Sanford, P. W., et al. 1976, MNRAS, 176, 201.